DE GRUYTER Nanophotonics 2021; 10(11): 2949–2958

Research article

Runcheng Liu, Zhipeng Zha, Muhammad Shafi, Can Li, Wen Yang, Shicai Xu, Mei Liu*
and Shouzhen Jiang*

Bulk plasmon polariton in hyperbolic metamaterials excited by multilayer nanoparticles for surface-enhanced Raman scattering (SERS) sensing

https://doi.org/10.1515/nanoph-2021-0301
Received June 15, 2021; accepted July 19, 2021;

Abstract: The capability to support large wave vector bulk plasmon polariton (BPP) waves enables the application of hyperbolic metamaterials (HMMs) in sensing. However, there is a challenge arising from the excitation of BPP, and the highly confined polarization waves are unable to meet the requirements of practical application. In this study, an HMM/bilayer silver nanoparticles (Ag NPs) platform is proposed that allows the excitation and utilization of BPP for use as a surface-enhanced Raman scattering (SERS) substrate. According to the research results, the bilayer Ag NPs provide stronger plasmonic property and act as a light-matter coupler, so as to generate a large wave vector of scattered light and excite the BPP within the HMM. Besides, Ag NPs provide the nano antenna structure, and decouple the BPP into localized surface plasmon (LSP) that can be used directly to excite the electric fields. In addition, HMM produces a modulating effect on the plasmon resonance peak, which makes it possible to overlap the spectrum of resonance peak with excitation wavelengths, thus leading to a strong absorption peak at the incident laser wavelength region. Experimentally, the platform was applied to achieve SERS detection for adenosine molecules with a concentration of 10^{-6} M. It is believed that this plasmonic platform has a potential of application in surface-enhanced spectroscopy.

Keywords: bulk plasmon polariton; hyperbolic metamaterials; surface-enhanced Raman scattering; surface plasmon polariton.

1 Introduction

The plasmon polariton achieved by the noble metal nanoparticles (NPs) in the process of light-matter interaction stimulates a strong local electric field and initiates the common optical process of surface-enhanced Raman scattering (SERS). It has been suggested for the detection of toxic and hazardous substances due to its advantage of being non-destructive, fast, label-free, and specific. The primary SERS mechanisms include electromagnetic mechanism (EM) and chemical mechanism (CM). As for EM, it relies on the local electric field originates from the localized surface plasmon (LSP) resonance effect of noble metal (Au, Ag, and Cu) [1]. This local electric field is further amplified at the plasmonic "hot spot" region of the gap between two NPs. In particular, when the gap falls below 10 nm, the electric field can reach 10^2–10^4 times that of a single NP [2]. As for CM, it relies on the charge transfer occurring between the SERS substrate and the probe

---

***Corresponding authors: Mei Liu and Shouzhen Jiang**, Collaborative Innovation Center of Light Manipulations and Applications in Universities of Shandong School of Physics and Electronics, Shandong Normal University, Jinan 250014, China; Shandong Key Laboratory of Medical Physics and Image Processing & Shandong Provincial Engineering and Technical Center of Light Manipulations, Jinan 250014, China, E-mail: liumei@sdnu.edu.cn (M. Liu), jiang_sz@126.com (S. Jiang).
Runcheng Liu, Zhipeng Zha, Muhammad Shafi and Can Li, Collaborative Innovation Center of Light Manipulations and Applications in Universities of Shandong School of Physics and Electronics, Shandong Normal University, Jinan 250014, China, E-mail: 380719609@qq.com (R. Liu), 2705663327@qq.com (Z. Zha), shafiicp@gmail.com (M. Shafi), lican753@163.com (C. Li). https://orcid.org/0000-0002-5267-7713 (R. Liu). https://orcid.org/0000-0002-0381-4646 (M. Shafi)
Wen Yang, School of Control Science and Engineering, Shandong University, Jingshi Road, 250061 Jinan, China, E-mail: wenyang0@126.com
Shicai Xu, Shandong Key Laboratory of Biophysics, College of Physics and Electronic Information, Institute of Biophysics, Dezhou University, Dezhou 253023, China, E-mail: shicaixu@dzu.edu.cn

molecules [3, 4]. This enhancement can be superimposed with EM to further improve Raman signal enhancement by 10–100 times [5].

Due to the dominance of EM in Raman enhancement, prior research has focused mainly on the generation of stronger hot spots, both in the intensity and density of the hot spots. Such tip-rich artificial structures as bowtie nanoantenna [6] and nanobowls [7, 8] have been proposed for the purpose of generating stronger LSP. Besides, such natural structures as cicada wings [9] and mussel shells [10] have also been reportedly processed for SERS because of their arrayed gap-rich structure. The above structures are intended to producing small gaps for the enhancement of hot spots. In addition, there have been various three-dimensional (3D) structures like multilayer nanocubes developed to increase the density of hot spot [11]. The multilayer NPs structure is usually formed by stacking monolayer NPs with two-dimensional (2D) materials as spacers. In this way, the distance between two adjacent layers of NPs can be precisely controlled to nanometers. The chemical enhancement of 2D materials also facilitates the enhancement of electric fields [4]. More importantly, both horizontal and vertical gaps within the multilayer structure can generate hot spots, thus enhancing the density of hot spots [12]. The LSPs of the NPs in each layer are coupled with each other, thus increasing the intensity of the topmost hot spot [11]. Therefore, the development of multilayer structures has attracted increasing attention in recent years.

In addition to the stacking of NPs, plasmon polariton can also be achieved by the stacking of metal/dielectric layers. When certain conditions on the materials and thickness of the multilayer structure are met, the structure demonstrates some extraordinary property, which is called hyperbolic metamaterial (HMM) [13, 14]. Not only does its hyperbolic dispersion curve support the propagation of surface wave along the metal surface, it also promotes the transmission of bulk wave among different layers [15]. As a result, the surface plasmon polariton (SPP) of each metal film surface leads to a Bloch mode through coupling [16]. This bulk plasmon polariton (BPP) is essential for SERS due to its capability to stimulate large electric fields [17]. In addition, HMM is used to enhance the optical absorption of analyte molecules at mid-infrared wavelengths for surface-enhanced infrared absorption (SEIRA) spectroscopy [18–20]. However, the large wave vector of BPP makes it difficult to stimulate and utilize [21]. Sreekanth et al. achieved the purpose of BPP excitation via a hypergrating structure formed by depositing a Ag film on a PMMA grating [22]. In addition, a 2D porous Au nanorod array was also produced to excite the BPP of HMM and then applied to plasmonic biosensors [23]. Maccaferri et al. proposed a hyperbolic meta-antenna to support the excitation of a localized hyperbolic Bloch-like plasmons [24]. However, the preparation of these structures is complex and sophisticated equipment is required. In addition, the number of layers of HMM can also affect the coupling of BPP. For 10 nm thick Au and Al_2O_3 multilayer structure, at least 4 pairs of metal/dielectric layers are needed to support the hyperbolic property, while the thicker layer cells require more periods due to the decay of the electric field [25]. These properties of HMM make it necessary to design the parameters for application carefully.

In this study, an HMM/multilayer Ag NPs platform is proposed to achieve the coupling of HMM and Ag NPs for application in SERS sensing. Firstly, various structures were designed and simulated to find out that the HMM/bilayer Ag NPs can produce the optimal plasmonic performance. The double-layered Ag NPs with graphene oxide (GO) as a spacer layer generates stronger LSP resonance and contributes to the coupling with the HMM. The GO layer also provides a chemical enhancement to the electric field. As suggested by the simulation of the electric field distribution of this nanostructure, the BPP can be excited. Subsequently, an analysis was conducted of the multiple coupling modes between the composite structures. According to the analytical results, the Ag NPs could decouple the BPP into the LSP, thus reinforcing the electric field outside the HMM. Besides, the HMM can modulate the band of the resonance peak to improve the plasmonic performance at the incident wavelength. Lastly, the Raman-enhanced performance of the platform was verified using adenosine molecules. It demonstrated a high capacity of detection in practice with a limit of detection (LOD) of 5.6×10^{-7} M and enhancement factor (EF) of 4.4×10^5.

2 Results and discussion

2.1 Theoretical design and analysis

The property of HMM are determined by the number of layers, materials, and filling ratio (volume ratio of metal to dielectric). In this study, there are 5 pairs of gold/alumina (Au/Al_2O_3) multilayer film structure chosen as HMM substrates (see Supplementary Note 1). Besides, in order to determine the optimal coupling conditions between Ag NPs and HMM, four different structures, including monolayer Ag NPs, bilayer Ag NPs, HMM/monolayer Ag NPs, and HMM/bilayer Ag NPs (marked as 1Ag, 2Ag, HMM/1Ag,

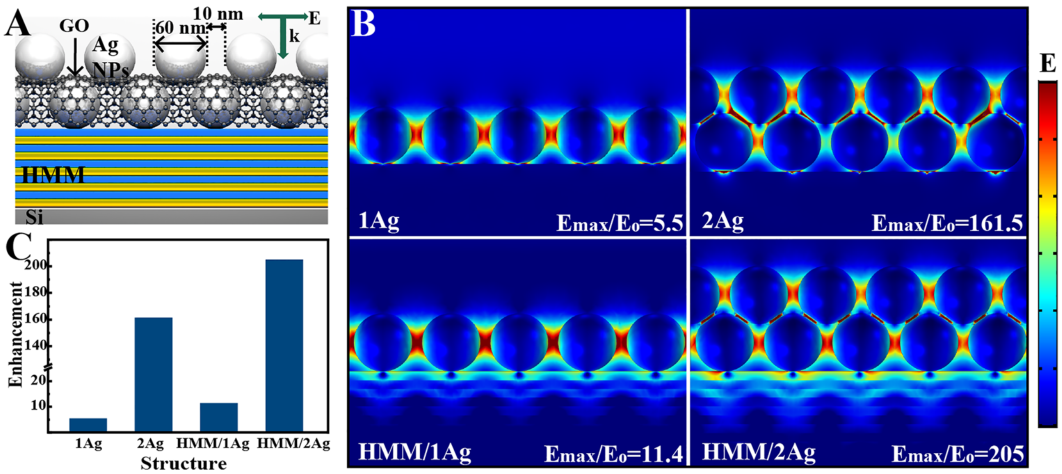

Figure 1: (A) Simulated composite nanostructure. Incident wavelength: 532 nm. (B) Electric field distribution of various structures. (C) Comparison of the simulated electric field enhancement of various structures.

and HMM/2Ag), were designed and simulated. The geometric parameters of the designed nanostructure are shown in Figure 1A. The simulation results shown in Figure 1B indicate the distribution of the electric field and the magnitude of the electric field enhancement (ratio of the maximum electric field intensity to the background electric field intensity). As for 1Ag, the hot spots are concentrated in the NP gap. The value of electric field enhancement denoted as E_{max}/E_0 is 5.5. For the 2Ag nanostructure, hot spots are concentrated in the vertical gap between the two layers of NPs, which is attributed to the smaller gap in the vertical direction and the further enhancement of GO. The level of electric field enhancement reaches 161.5. In the horizontal direction, the hot spots between the upper NPs are stronger than that of the lower NPs, which results from the attenuation of the incident laser. Consequently, the utilization of the HMM leads to a sharp increase in the intensity of electric field. Notably, distinct from the case of 2Ag, the intensity of electric field for the bottom NPs is higher as compared to the upper NPs for HMM/2Ag. While the intensity of electric field within the HMM declines from the top to the bottom, suggesting that the HMM contributes to further enhancing electric field in the composite system and that the enhancement reaches its maximum at the interface between the NPs and HMM [26].

Figure 1C shows the comparison of electric field enhancement between various structures. To be specific, the enhancement of 2Ag, HMM/1Ag, and HMM/2Ag is 29.3, 2, and 37.3 times that of 1Ag, respectively, indicating that the stacking of Ag NPs plays a much more significant role in the enhancement than the HMM. Therefore, a study was conducted on the performance of a three-layer Ag NPs structure (Supplementary Note 2). The excessively thick Ag NPs not only affects the laser incidence but also inhibits the coupling of NPs and HMM [11]. In contrast, there is a less significant Raman enhancement effect. Therefore, HMM/2Ag can be treated as the optimal plasmonic structure for the excitation and application of BPP.

Apparently, the hot spots within the HMM are concentrated in the Al_2O_3 layer. The polariton of this form, as supported between the two metal layers, is referred to as gap plasmon polariton (GPP) [27], which plays a vitally important role in enhancing the electric field [28]. In order to analyze the mode of polariton within the HMM, an Au nanoblock was prepared as a comparison. A 45 nm thick gold layer and a 9 nm thick Al_2O_3 layer were deposited on the Si wafer to ensure the same Au thickness as the HMM structure (Figure S1A). As revealed by the Raman spectra shown in Figure S1B, HMM shows a higher intensity of Raman signal than Au nanoblock. Subsequently, simulation was conducted to provide theoretical support for this phenomenon. Figure 2A_1 and B_1 shows the distribution of electric field and the field profile of the Au nanoblock under the context of 66° incident laser irradiation. There is an insignificant enhancement observed within the Au film and a significant enhancement found at the Au/Al_2O_3 interfaces. Such an elevation of the electric field is attributable to the excitation of the SPP. Typically, the SPP is confined to within a tenth of a nanometer from the interface, as a result of which the magnitude of the electric field elevation is small within the Au nanoblock [29]. As for the HMM, the 9 nm thickness of Au and Al_2O_3 film facilitates the propagation of the SPP and the generation of GPP, thus enhancing the electric fields (Figure 2A_2). The GPP has a larger wave vector, which results in a stronger electric field

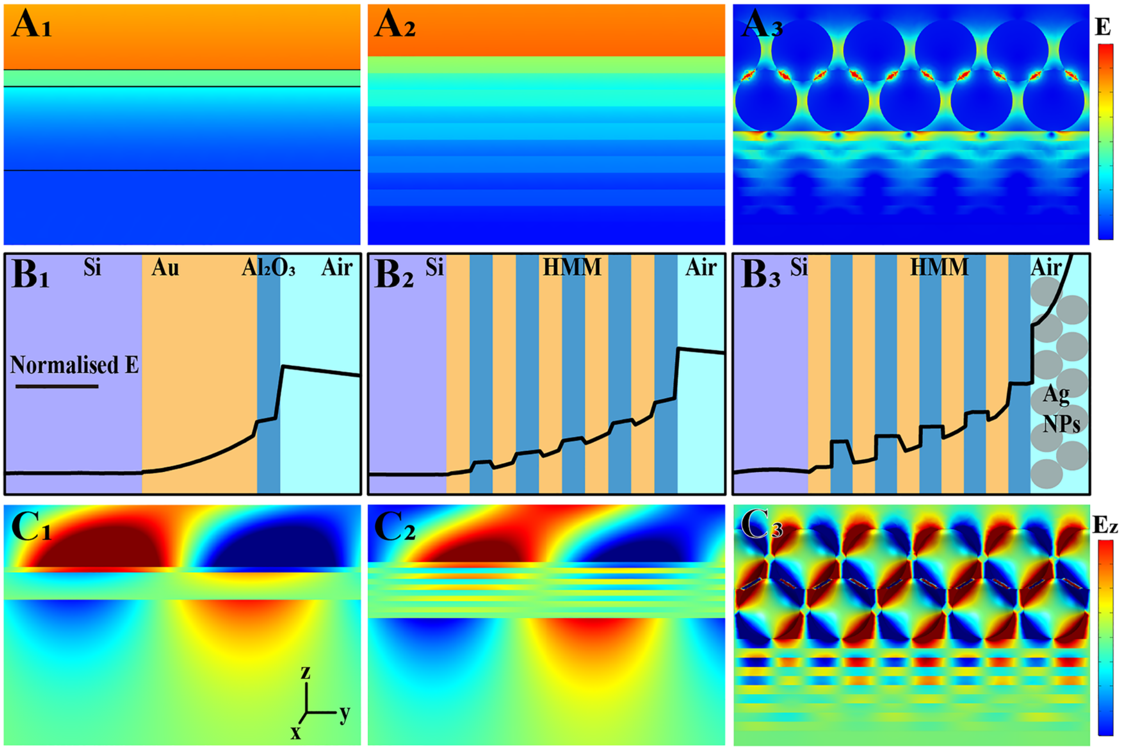

Figure 2: (A) Electric field distribution for Au nanoblock, hyperbolic metamaterial (HMM) and HMM/2Ag. (B) Field profile for various structures. (C) Diagram of the propagation of the Ez field (multimedia files).

confinement effect. Consequently, the elevation of the electric field occurs within the Al_2O_3 dielectric layer (Figure $2B_2$). Moreover, the GPPs can be coupled to form a BPP, which is favorable to interlayer propagation [15, 16]. However, either large angular incidence light or other coupling conditions are required to match the wave vector for BPP excitation [21, 30]. Besides, the severely confined property of the BPP cause it does not contribute to the field enhancement outside of HMM, which makes it difficult to generate hot spots at the probe molecule region [17, 31]. These two issues limit the practical application of HMM in SERS.

With Ag NPs as an external source of excitation and an antenna-like structure, the above-mentioned problems can be solved effectively. Scattered by the array of Ag NPs, the wave vector of the incident light increases to match that of the BPP (Supplementary Note 3) [32–35]. Therefore, the BPP of the HMM can still be excited under the excitation of a vertically incident laser, as shown in Figure $2A_3$. Furthermore, this antenna-like structure decouples the BPP confined within the HMM into LSP [26], while the electric field originally bound to the interface also expands into the NPs gap. In addition, the propagation diagram of the z-component of the electric field “Ez” for each structure is plotted in Figure 2C. The Ez field for both the Au nanoblock and the HMM behaves as a surface wave mode, which propagate along the interface in the direction of incident light polarization. In contrast, HMM/2Ag exhibits the Ez field propagating between the layers and into the NPs. Further, we analyzed the Ez field profile of the HMM/2Ag (Figure S2), which exhibits the oscillatory mode of the BPP as well as the high confined property [27, 36]. These phenomena demonstrate that the BPP has been excited and contributes a generous electric field to the Ag NPs.

In addition to field confined and field enhancement, another characteristic of HMM is the modulation of resonance peak. Figure 3A shows the absorption spectra of Ag NPs, Au nanoblock, HMM, and HMM/2Ag, respectively. Ag NPs have a narrow peak at about 350 nm. Au nanoblock has a peak at about 450 nm. In contrast, HMM shows a broad absorption peak at about 600 nm. The broad absorption peaks are due to the weak surface plasmon resonance under the irradiation of vertically incident light. While the Al_2O_3 makes the resonance wavelength of HMM red-shifted relative to the Au nanoblock [37]. Notably, the HMM/2Ag structure exhibits multiple absorption peaks (marked by arrows). In addition to the absorption peaks resulting from the Ag NPs, the higher-order BPP is also contributory to these peaks [22, 23]. In general, the more significant resonance absorption suggests stronger plasmonic property [37]. Moreover, the absorption of the system contributes to the coupling of the NPs and HMM [38]. Therefore, the intensity of electric field for each structure at different excitation wavelengths was simulated. In Figure 3B, the electric field strength profile is highly consistent with the absorption spectrum for Ag NPs, with a maximum of 350 nm. The profile of the HMM/2Ag structure displayed four local maxima, corresponding to the four absorption peaks in the absorption spectrum. The intensity of electric field for the HMM/2Ag structure is higher compared with Ag NPs after 450 nm, suggesting a modulation effect of the HMM on the resonance peak. A strong absorption is generated in an otherwise inactive band. Moreover, Figure 3C shows the distribution of electric field for the HMM/2Ag structure at the three commonly used excitation wavelengths of 325, 532, and 785 nm, respectively. In addition to the variation in electric field intensity, there are also differences in the distribution of electric field. Under the excitation at 325 nm, the multilayer structure falls in the effective dielectric region and shows no hyperbolic property (Figure 3C). Only weak electric fields are concentrated on the surface of the nanostructure, which suggests that the LSP and BPP are not excited. Under the excitation at 785 nm, the intensity of electric field for both the Ag NPs and the HMM is elevated, but not to a significant extent at the HMM/NPs interface, which indicates a weak coupling effect. Differently, a significant coupling effect plays out at 532 nm, the wavelength closest to the absorption peak. With this property, it is expected to achieve not only the modulation of the resonance peak but also the joint enhancement of the incident and scattered electric fields in the SERS [39–41].

2.2 Sample characterization

After the theoretical design, various nanostructures were prepared experimentally. Figure 4A and B shows the cross-sectional and top views of morphology of the prepared HMM. The bright Au and the dark Al_2O_3 films are found continuous and uniform on a large scale, with clear demarcation lines observed. As indicated by the atomic force microscopy (AFM) height profile of the HMM surface (Figure S3A), the structure has a root-mean-square (RMS) roughness of 0.59 nm, which is conducive to ensuring an ideal plasmonic performance of the platform [42]. The height profile (Figure 4C) indicates a thickness of 93.4 nm for the HMM layer, which is basically consistent with the expected thickness of 90 nm. Figure 4D and E presents the

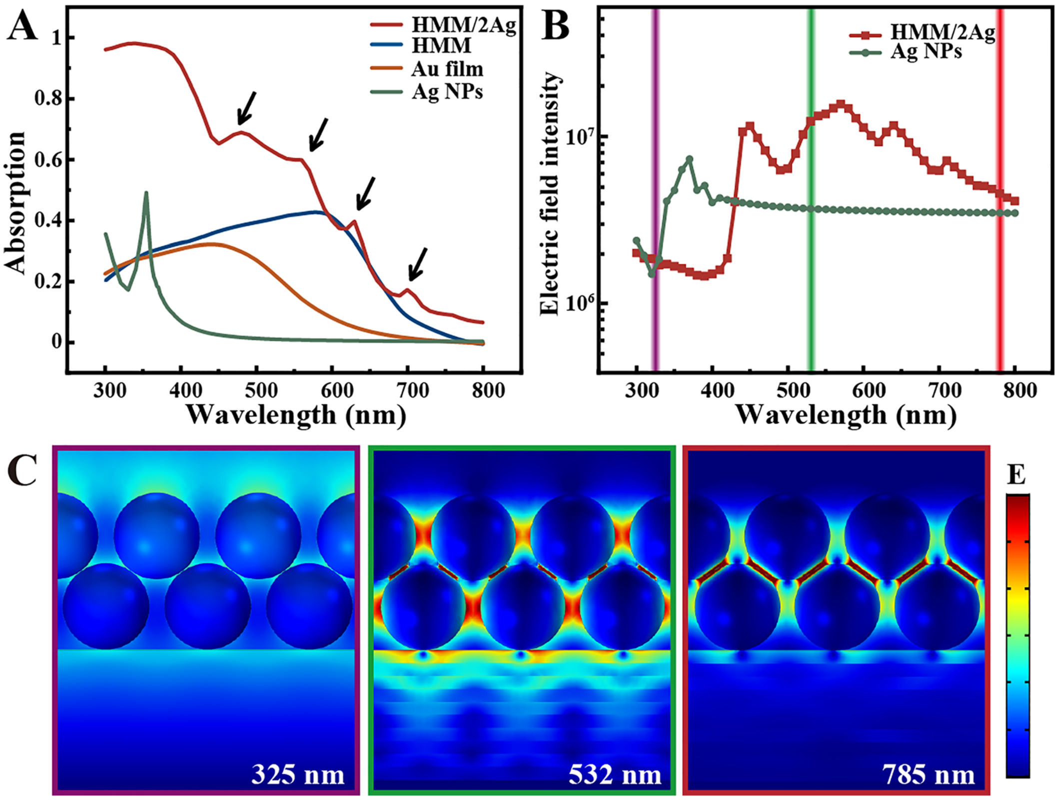

Figure 3: (A) The simulated absorbance spectra of various nanostructures. (B) Simulated electric field intensity of Ag NPs and HMM/2Ag versus the excitation wavelength. (C) Electric field distribution of HMM/Ag nanostructure on the excitation wavelength of 325, 532, and 785 nm, respectively.

morphology of the prepared monolayer Ag NPs and the nanostructure of bilayer Ag NPs. The Ag NPs are uniform in size (average diameter of about 57 nm) and evenly distributed at a spacing of about 10 nm. With regard to the structure of bilayer Ag NPs, both the upper and lower NPs are well distributed due to the spacing of GO, without any sign of agglomeration. The wrapping of GO makes the lower layer of Ag NPs darker and blurred to some extent, which allows the easy identification of the bilayer nanostructure. In order to improve the effectiveness of characterizing the bilayer nanostructure as well as the GO, transmission electron microscopy (TEM) measurements were performed. In Figure 4F, the stacking of bilayer NPs can be observed in the marked area and the GO wrinkles are also visible in the area indicated by the arrow. As shown in Figure S3B, the thickness of GO is approximately 3.5 nm, which ensures not only the support of the upper Ag NPs but also the strong LSP coupling between bilayer NPs. For comparison purpose, the bilayer Ag NPs without GO spacer were prepared and studied (Supplementary Note 4). In the absence of a separating layer, the NPs tend to stack densely rather than forming a layered structure, which has adverse effect on LSP [43].

In addition, the composition of the nanostructures was determined by X-ray photoelectron spectroscopy (XPS) spectroscopy. The survey spectrum of the HMM/2Ag substrate is shown in Figure 5A, where the characteristic peaks for Au, Ag, and Al_2O_3 are observable. Meanwhile, the high-resolution spectra of Au 4f and Ag 3d are shown in Figure 5B and C, respectively. The peaks of Au $4f_{5/2}$, Au $4f_{7/2}$, Ag $3d_{3/2}$, and Ag $3d_{5/2}$ promoted the insertion of crystallized Au and Ag. Notably, the peak at 74.6 eV as shown in Figure 5D is assigned to the Al 2p orbital of Al^{3+} ions derived from Al_2O_3, which suggests that the Al metal has been oxidized as anticipated.

With the R6G at a concentration of 10^{-6} M as probe molecule, the plasmonic performance of 1Ag, 2Ag, HMM/1Ag, and HMM/2Ag structures was characterized. According to the Raman spectra shown in Figure 6A, the HMM/2Ag composite structure releases the strongest Raman signal. The intensity contrast graph presented in Figure 6B shows variation in the intensity of Raman signal between the individual structures. The disparity in enhancement performance for 613, 1364, and 1651 cm^{-1} peaks is attributed to the difference in adsorption pattern of the molecules on the individual substrates, which has no impact on the subsequent analysis [44]. The monolayer Ag NPs shows the weakest signal. Comparatively, the intensity of signal for 2Ag and HMM/Ag is 1.7 times higher than that of 1Ag. With the dual enhancement of the HMM and the Ag NPs, the intensity of signal can reach up to 2.4 times the original level, which implies the occurrence of coupling between the Ag NPs and HMM. It is worthwhile to be noted that despite the structural deficiencies in the actual experiment make the experimentally enhanced results weaker than the simulation results shown in Figure 1C, there is a consistent variation between the experiments and simulations.

2.3 SERS performance measurement

Due to the bioavailability of Ag and GO, the SERS substrate (Figure 7A) can be applied to assist biomolecular detection.

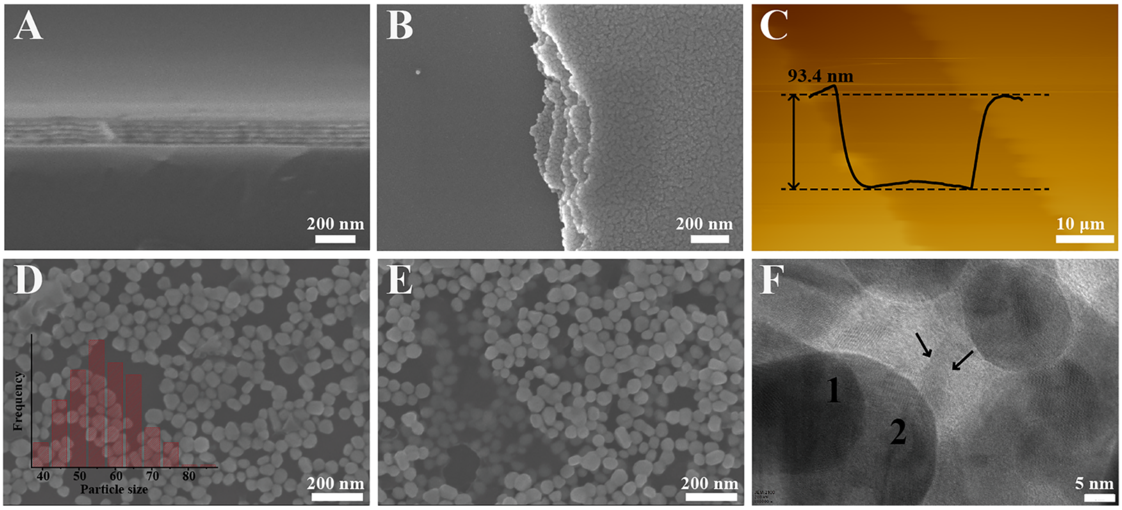

Figure 4: (A) Cross-sectional and (B) top view scanning electron microscope (SEM) images of hyperbolic metamaterial (HMM). (C) Atomic force microscopy (AFM) image of the HMM and the corresponding height profile. SEM images of (D) 1Ag and (E) 2Ag. Insert is the size distribution histograms of Ag NPs. (F) Transmission electron microscopy (TEM) image of bilayer Ag NPs structure.

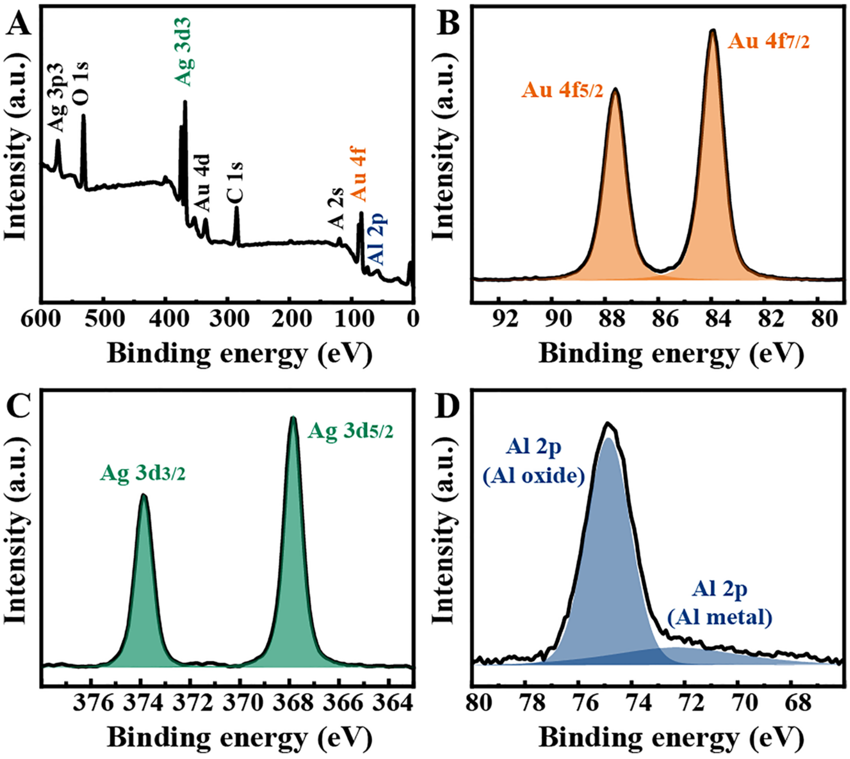

Figure 5: X-ray photoelectron spectroscopy (XPS) spectra in (A) survey, (B) Au 4f, (C) Ag 3d, and (D) Al 2p regions of HMM/2Ag substrate.

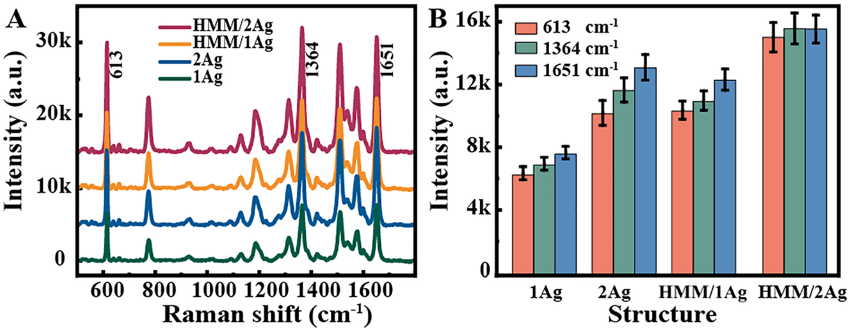

Figure 6: (A) Raman spectra of R6G molecules (10^{-6} M) detected from 1Ag, 2Ag, HMM/1Ag, and HMM/2Ag. (B) The intensity of the R6G at 613, 1364, and 1651 cm^{-1} peaks detected in various substrates.

Herein, adenosine was taken as the probe molecule for Raman detection. Figure 7B shows the Raman spectra of adenosine molecules with varying concentrations and adenosine powder. The main characteristic peaks of adenosine powder are located at 722 and 1332 cm^{-1}, respectively. The Raman peak at 1333 cm^{-1} indicates the in-plane oscillation vibration of the C–H and N–H bonds as well as the in-plane stretching vibration of the C–N bond inside the purine ring molecule. When the Ag^+ ions are bound to the N3 or N9 site of adenosine, the peak at 723 cm^{-1} shifts to 739 cm^{-1} [45]. The presence of these peaks is essential for the quantitative analysis of adenosine molecules. In the spectrogram, the characteristic peaks remained easily distinguishable at the concentrations down to 1×10^{-6} M. In contrast, the control substrate with the addition of deionized water displayed only spurious peaks from the Ag colloid. To better demonstrate the quantitative detection capability of the substrate, two peaks, 722 and 1332 cm^{-1}, were selected to analyze the intensity of their Raman signal against concentration. The calibration curves are presented in Figure 7C, exhibiting a linear relationship with a R^2 of 0.994 for 736 cm^{-1} peak and 0.986 for 1333 cm^{-1} peak. The LOD was determined as 5.6×10^{-7} M using the formula: LOD = 3(SD/S) (see Supplementary Note 5 for details) [46]. To assess the uniformity of the substrate, the Raman mapping of 736 cm^{-1} peak was collected from an area of $20 \times 20\ \mu\mathrm{m}^2$ on the substrate (Figure 7D). The relative standard deviation (RSD) was calculated to be 12%, indicating excellent uniformity. Moreover, 10 random spots were taken from each of the 10

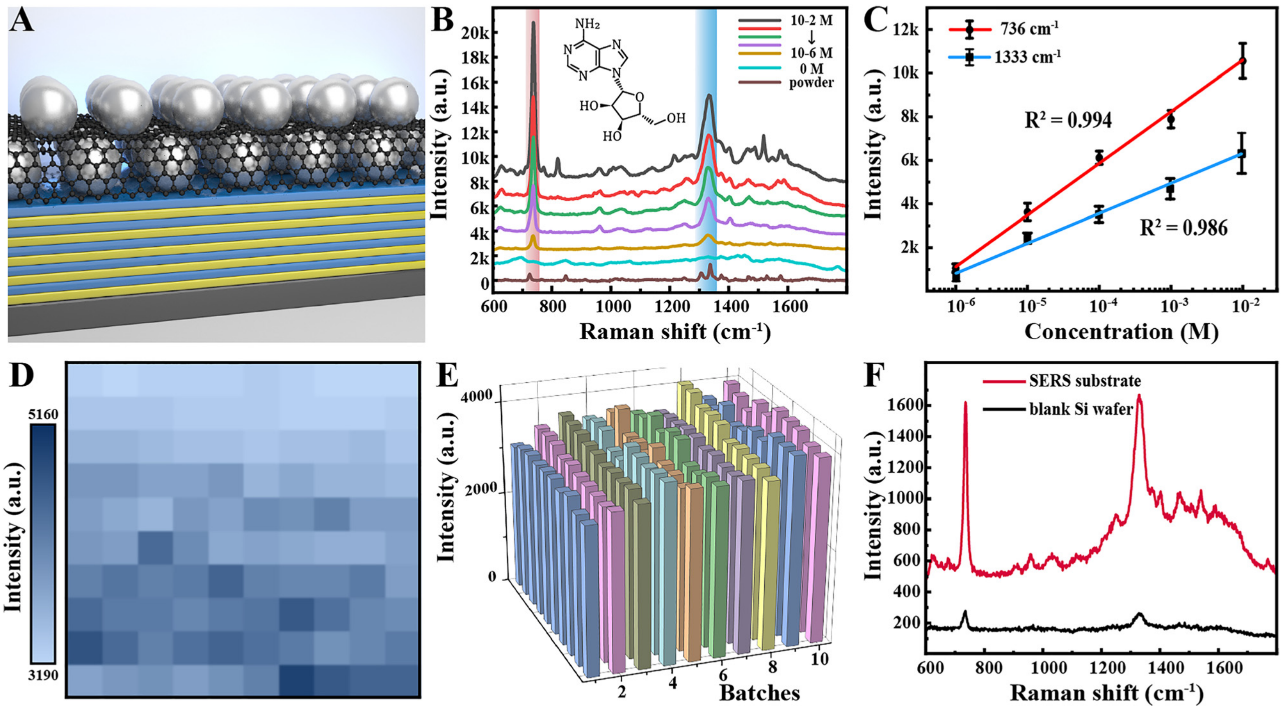

Figure 7: (A) Schematic diagram of the surface-enhanced Raman scattering (SERS) substrate. (B) Raman spectra of varying concentrations of adenosine. (C) The calibration curve of Raman intensity at different concentrations. (D) Raman mapping with an area of 20 × 20 μm^2 for 736 cm^{-1} peak. (E) The intensity of 736 cm^{-1} peak collected from 10 spots on each of 10 batches of substrates. (F) Raman spectrum of adenosine (10^{-6} M) on SERS substrates and the spectrum of adenosine (10^{-2} M) on blank Si wafer.

batches of substrates and the intensity of their signal is shown in Figure 7E. The insignificant variation between batches evidences the strong reproducibility of the substrate. In order to estimate the SERS performance of the substrate in detail, the EF of adenosine was calculated using the following formula [47].

$$\mathrm{EF} = \frac{I_{\mathrm{SERS}} \times N_{\mathrm{Raman}}}{I_{\mathrm{Raman}} \times N_{\mathrm{SERS}}} \tag{1}$$

With the corresponding values substituted, the EF of the SERS substrate was calculated to be nearly 4.4×10^5 (see Supplementary Note 5 for details).

3 Conclusion

In summary, with Ag NPs as external coupling conditions, the excitation of BPP was performed within the HMM for application in SERS sensing. As an ideal LSP excitation source, a bilayer of Ag NPs with GO as a spacer layer was used to achieve the large wave vector polarization wave that satisfied the wave vector matching condition of BPP. The excited BPP was decoupled by the Ag NPs, thus leading to a 205-fold enhancement of the electric field at the interparticle interval. In addition, the different orders of BPP contributed to multiple resonance modes, thus modulating the single absorption peak originally located at ~350 nm into multiple absorption peaks after 450 nm. Ultimately, a stronger plasmon resonance of the substrate was triggered in the visible region. Due to the above reasons, the substrate performed well in detecting adenosine molecules. At the excitation wavelength of 532 nm, it has a LOD of 5.6×10^{-7} M and an EF of 4.4×10^5. The proposed HMM/particle platform lays foundation for the extensive HMM-based applications in the field of surface-enhanced spectroscopy.

4 Experimental section

4.1 Materials

Both alcohol (C_2H_6O, 99.7%) and acetone (CH_3COCH_3, 99.5%) were purchased from a local chemical plant. Ag and Al targets were sourced from Fuzhou Invention photoelectrical Tech Co., Ltd. Ag colloid (1 mg/mL) and GO dispersion (0.5 mg/mL) were provided by Nanjing XFNANO Materials Tech Co., Ltd.

4.2 Preparation of HMM and multilayer AgNPs

In order to obtain the desired structure, Si wafer was washed using acetone, ethanol, and deionized water continuously with the assistance of ultrasonic cleaner for 1 h to remove the organic pollutants. Afterwards, a 9 nm thick Au film was deposited on the Si wafer by means of vacuum thermal evaporation (0.1 Å/s, 7×10^{-5} Pa). The 9 nm thick Al_2O_3 film was obtained by repeating the process of evaporating the 3 nm Al film (0.5 Å/s, 7×10^{-5} Pa) and oxidizing it in pure oxygen for three times. To carry out the oxidation of the Al film, the sample was placed in a vacuum kettle and evacuated to 1×10^3 Pa, and pure oxygen was introduced and then held for 10 min. After the repeated deposition of Au and Al_2O_3 layers, a 5-period HMM structure was obtained. Then, multilayer NPs were prepared on the HMM and the Si wafer, respectively. After Ag colloid was dropped on the as-prepared HMM to dry naturally, GO was dropped on the Ag NPs and spin-coated at 2000 rpm for 30 s. The repeated drops of Ag colloid and GO were used to obtain a multilayer NPs structure.

4.3 Sample characterization and SERS experiments

The morphology of each substrate was examined by SEM (Zeiss Gemini Ultra-55). The surface chemistry, composition, and valence state of the prepared substrate were characterized by XPS (Thermo Fisher Scientific 250Xi). The multilayer structure of the NPs was studied using TEM (JEM-2100). The thickness of the sample was measured by AFM (Horiba SmartSPM). Raman spectrometer (Horiba HR Evolution) was applied to capture the Raman signals. All of the Raman spectra were obtained using a 532 nm exciting laser, with 600 grooves per 1 mm, ×50 objective lens, 1 μm laser spot, and 4 s of acquisition time.

5 Supplementary material

Au nanoblock image; Ez field profile; AFM image; theory and determination of HMM; study of triple-layer Ag NPs; Analysis of dispersion curves; the role of GO in multilayer NPs; details of LOD and EF calculation; multimedia files in Figure 2.

Acknowledgments: Great thanks to Qianqian Peng for her helpful suggestion in our SEM characterization.

Author contributions: All the authors have accepted responsibility for the entire content of this submitted manuscript and approved submission.

Research funding: The authors acknowledge the support from the National Natural Science Foundation of China (NSFC) (12074226, 12074229, 11674199, and 12004226) (http://dx.doi.org/10.13039/501100001809), Taishan Scholar Project of Shandong Province (http://dx.doi.org/10.13039/501100010040) (tsqn201812104) and Qingchuang Science and Technology Plan of Shandong Province (2019KJJ017).

Conflict of interest statement: The authors declare no conflict of interest.

References

[1] X. Wang, S.-C. Huang, S. Hu, et al., “Fundamental understanding and applications of plasmon-enhanced Raman spectroscopy,” *Nat. Rev. Phys.*, vol. 2, pp. 253–271, 2020.

[2] S.-Y. Ding, J. Yi, J.-F. Li, et al., “Nanostructure-based plasmon-enhanced Raman spectroscopy for surface analysis of materials,” *Nat. Rev. Mater.*, vol. 1, p. 16021, 2016.

[3] X. Ling, L. Xie, Y. Fang, et al., “Can graphene be used as a substrate for Raman enhancement?” *Nano Lett.*, vol. 10, pp. 553–561, 2010.

[4] X. Ling, W. Fang, Y.-H. Lee, et al., “Raman enhancement effect on two-dimensional layered materials: graphene, h-BN and MoS2,” *Nano Lett.*, vol. 14, pp. 3033–3040, 2014.

[5] J. Langer, D. Jimenez de Aberasturi, J. Aizpurua, et al., “Present and future of surface-enhanced Raman scattering,” *ACS Nano*, vol. 14, pp. 28–117, 2020.

[6] Z. Dai, X. Xiao, L. Liao, et al., “Large-area, well-ordered, uniform-sized bowtie nanoantenna arrays for surface enhanced Raman scattering substrate with ultra-sensitive detection,” *Appl. Phys. Lett.*, vol. 103, p. 041903, 2013.

[7] X. Zhang, X. Zhang, C. Luo, et al., “Volume-enhanced Raman scattering detection of viruses,” *Small*, vol. 15, p. 1805516, 2019.

[8] P. Mao, C. Liu, G. Favraud, et al., “Broadband single molecule SERS detection designed by warped optical spaces,” *Nat. Commun.*, vol. 9, p. 5428, 2018.

[9] W. Yang, Z. Li, Z. Lu, et al., “Graphene-Ag nanoparticles-cicada wings hybrid system for obvious SERS performance and DNA molecular detection,” *Opt. Express*, vol. 27, pp. 3000–3013, 2019.

[10] Z. Lu, Y. Liu, M. Wang, et al., “A novel natural surface-enhanced Raman spectroscopy (SERS) substrate based on graphene oxide-Ag nanoparticles-Mytilus coruscus hybrid system,” *Sens. Actuators B Chem.*, vol. 261, pp. 1–10, 2018.

[11] Z. Li, S. Jiang, Y. Huo, et al., “3D silver nanoparticles with multilayer graphene oxide as a spacer for surface enhanced Raman spectroscopy analysis,” *Nanoscale*, vol. 10, pp. 5897–5905, 2018.

[12] X. Xiu, L. Hou, J. Yu, et al., “Manipulating the surface-enhanced Raman spectroscopy (SERS) activity and plasmon-driven catalytic efficiency by the control of Ag NP/graphene layers under optical excitation,” *Nanophotonics*, vol. 10, pp. 1529–1540, 2021.

[13] Z. Dai, G. Hu, Q. Ou, et al., "Artificial metaphotonics born naturally in two dimensions," *Chem. Rev.*, vol. 120, pp. 6197–6246, 2020.

[14] A. Poddubny, I. Iorsh, P. Belov, et al., "Hyperbolic metamaterials," *Nat. Photon.*, vol. 7, pp. 948–957, 2013.

[15] L. Ferrari, C. Wu, D. Lepage, et al., "Hyperbolic metamaterials and their applications," *Prog. Quantum Electron.*, vol. 40, pp. 1–40, 2015.

[16] Y. Guo, W. Newman, C. L. Cortes, et al., "Applications of hyperbolic metamaterial substrates," *Adv. Optoelectron.*, vol. 2012, p. 452502, 2012.

[17] A. Bruno-Alfonso, E. Reyes-Gómez, S. B. Cavalcanti, et al., "Field profiles of bulk plasmon polariton modes in layered systems containing a metamaterial," *J. Phys. Condens. Matter*, vol. 24, p. 045302, 2012.

[18] T. G. Folland, G. Lu, A. Bruncz, et al., "Vibrational coupling to epsilon-near-zero waveguide modes," *ACS Photonics*, vol. 7, pp. 614–621, 2020.

[19] E. Shkondin, T. Repän, M. E. Aryaee Panah, et al., "High aspect ratio plasmonic nanotrench structures with large active surface area for label-free mid-infrared molecular absorption sensing," *ACS Appl. Nano Mater.*, vol. 1, pp. 1212–1218, 2018.

[20] M. Autore, P. Li, I. Dolado, et al., "Boron nitride nanoresonators for phonon-enhanced molecular vibrational spectroscopy at the strong coupling limit," *Light Sci. Appl.*, vol. 7, p. 17172, 2018.

[21] M. Mahmoodi, S. H. Tavassoli, O. Takayama, et al., "Existence conditions of high-k modes in finite hyperbolic metamaterials," *Laser Photonics Rev.*, vol. 13, p. 1800253, 2019.

[22] K. V. Sreekanth, A. De Luca, and G. Strangi, "Experimental demonstration of surface and bulk plasmon polaritons in hypergratings," *Sci. Rep.*, vol. 3, p. 3291, 2013.

[23] K. V. Sreekanth, Y. Alapan, M. ElKabbash, et al., "Extreme sensitivity biosensing platform based on hyperbolic metamaterials," *Nat. Mater.*, vol. 15, pp. 621–627, 2016.

[24] N. Maccaferri, Y. Zhao, T. Isoniemi, et al., "Hyperbolic meta-antennas enable full control of scattering and absorption of light," *Nano Lett.*, vol. 19, pp. 1851–1859, 2019.

[25] J. Sukham, O. Takayama, M. Mahmoodi, et al., "Investigation of effective media applicability for ultrathin multilayer structures," *Nanoscale*, vol. 11, pp. 12582–12588, 2019.

[26] J. A. Girón-Sedas and F. J. Rodríguez-Fortuño, "Strong recoil optical forces on dipoles via high-k plasmons excitation in thin metallic films," *Appl. Phys. Lett.*, vol. 117, p. 181106, 2020.

[27] I. Avrutsky, I. Salakhutdinov, J. Elser, et al., "Highly confined optical modes in nanoscale metal-dielectric multilayers," *Phys. Rev. B*, vol. 75, p. 241402, 2007.

[28] H. T. Miyazaki and Y. Kurokawa, "Squeezing visible light waves into a 3-nm-thick and 55-nm-long plasmon cavity," *Phys. Rev. Lett.*, vol. 96, p. 097401, 2006.

[29] W. L. Barnes, A. Dereux, and T. W. Ebbesen, "Surface plasmon subwavelength optics," *Nature*, vol. 424, pp. 824–830, 2003.

[30] J. Chen, P. Wang, X. Wang, et al., "Optical bistability enhanced by highly localized bulk plasmon polariton modes in subwavelength metal-nonlinear dielectric multilayer structure," *Appl. Phys. Lett.*, vol. 94, p. 081117, 2009.

[31] O. Kidwai, S. V. Zhukovsky, and J. E. Sipe, "Effective-medium approach to planar multilayer hyperbolic metamaterials: strengths and limitations," *Phys. Rev. A*, vol. 85, p. 053842, 2012.

[32] R. Liu, Z. Zha, C. Li, et al., "Coupling of multiple plasma polarization modes in particles–multilayer film system for surface-enhanced Raman scattering," *APL Photonics*, vol. 6, p. 036104, 2021.

[33] A. Akjouj, G. t. Lévêque, S. Szunerits, et al., "Nanometal plasmon polaritons," *Surf. Sci. Rep.*, vol. 68, pp. 1–67, 2013.

[34] Z. Zha, R. Liu, W. Yang, et al., "Surface-enhanced Raman scattering by the composite structure of Ag NP-multilayer Au films separated by Al_2O_3," *Opt. Express*, vol. 29, pp. 8890–8901, 2021.

[35] E. Devaux, T. W. Ebbesen, J.-C. Weeber, et al., "Launching and decoupling surface plasmons via micro-gratings," *Appl. Phys. Lett.*, vol. 83, pp. 4936–4938, 2003.

[36] M. Higuchi and J. Takahara, "Plasmonic interpretation of bulk propagating waves in hyperbolic metamaterial optical waveguides," *Opt. Express*, vol. 26, pp. 1918–1929, 2018.

[37] W. Chen, S. Zhang, M. Kang, et al., "Probing the limits of plasmonic enhancement using a two-dimensional atomic crystal probe," *Light Sci. Appl.*, vol. 7, p. 56, 2018.

[38] Y. Kalachyova, D. Mares, V. Jerabek, et al., "The effect of silver grating and nanoparticles grafting for LSP–SPP coupling and SERS response intensification," *J. Phys. Chem. C*, vol. 120, pp. 10569–10577, 2016.

[39] C.-H. Lai, G.-A. Wang, T.-K. Ling, et al., "Near infrared surface-enhanced Raman scattering based on star-shaped gold/silver nanoparticles and hyperbolic metamaterial," *Sci. Rep.*, vol. 7, p. 5446, 2017.

[40] Y. Chu, D. Wang, W. Zhu, et al., "Double resonance surface enhanced Raman scattering substrates: an intuitive coupled oscillator model," *Opt. Express*, vol. 19, pp. 14919–14928, 2011.

[41] M. Shioi, H. Jans, K. Lodewijks, et al., "Tuning the interaction between propagating and localized surface plasmons for surface enhanced Raman scattering in water for biomedical and environmental applications," *Appl. Phys. Lett.*, vol. 104, p. 243102, 2014.

[42] J. Sukham, O. Takayama, A. V. Lavrinenko, et al., "High-quality ultrathin gold layers with an APTMS adhesion for optimal performance of surface plasmon polariton-based devices," *ACS Appl. Mater. Interfaces*, vol. 9, pp. 25049–25056, 2017.

[43] M. Shafi, R. Liu, Z. Zha, et al., "Highly efficient SERS substrates with different Ag interparticle nanogaps based on hyperbolic metamaterials," *Appl. Surf. Sci.*, vol. 555, p. 149729, 2021.

[44] J. Zhao, L. Jensen, J. Sung, et al., "Interaction of plasmon and molecular resonances for rhodamine 6G adsorbed on silver nanoparticles," *J. Am. Chem. Soc.*, vol. 129, pp. 7647–7656, 2007.

[45] L. Wu, F. Li, Z. Y. Jin, et al., "The research on Raman spectroscopy of nucleic acid bases based on DFT method," *Prog. Biochem. Biophys.*, vol. 43, pp. 281–290, 2016.

[46] A. Shrivastava and V. B. Gupta, "Methods for the determination of limit of detection and limit of quantitation of the analytical methods," *Chron. Young Sci.*, vol. 2, pp. 15–21, 2011.

[47] E. C. Le Ru, E. Blackie, M. Meyer, et al., "Surface enhanced Raman scattering enhancement factors: a comprehensive study," *J. Phys. Chem. C*, vol. 111, pp. 13794–13803, 2007.

Supplementary material: The online version of this article offers supplementary material (https://doi.org/10.1515/nanoph-2021-0301).